Anisotropic effects in surface acoustic wave propagation from a point source in a crystal

A.A. Maznev[1,a], A.M. Lomonosov[2,b], P. Hess[2], and Al.A. Kolomenskii[3]

[1] Philips Advanced Metrology Systems, 12 Michigan Dr., Natick, MA 01760, USA
[2] Institut of Physical Chemistry, University of Heidelberg, Im Neuenheimer Feld 253, 69120 Heidelberg, Germany
[3] Department of Physics, Texas A&M University, College Station, TX 77843, USA

Abstract. Strong anisotropic effects in the propagation of surface acoustic waves (SAWs) from a point-like source are studied experimentally and theoretically. Nanosecond SAW pulses are generated by focused laser pulses and detected with a cw probe laser beam at a large distance from the source compared to the SAW wavelength, which allows us to resolve fine intricate features in SAW wavefronts. In our theoretical model, we represent the laser excitation by a localized impulsive force acting on the sample surface and calculate the far-field surface response of an elastically anisotropic solid to such a force. The model simulates the measured SAW waveforms very well and accounts for all experimentally observed features. Using the data obtained for the (111) and (001) surfaces of GaAs, we describe a variety of effects encountered in the SAW propagation from a point source in crystals. The most interesting phenomenon is the existence of cuspidal structures in SAW wavefronts resulting in multiple SAW arrivals for certain ranges of the observation angle. Cuspidal edges correspond to the "phonon focusing" directions yielding sharp peaks in the SAW amplitude. A finite SAW wavelength results in "internal diffraction" whereby the SAW wavefront spreads beyond the group velocity cusps. Degeneration of a SAW into a transverse bulk wave is another strong effect influencing the anisotropy of the SAW amplitude and making whole sections of the SAW wavefront including some phonon focusing directions unobservable in the experiment. The propagation of a leaky SAW mode (pseudo-SAW) is affected by a specific additional effect *i.e.* anisotropic attenuation. We also demonstrate that many of the discussed features are reproduced in "powder patterns", a simple technique developed by us earlier for visualization of SAW amplitude anisotropy.

PACS. 43.35.+d Ultrasonics, quantum acoustics, and physical effects of sound – 68.35.Gy Mechanical properties; surface strains – 62.65.+k Acoustical properties of solids

1 Introduction

In an elastically anisotropic solid, acoustic group and phase velocities are in general not collinear [1]. The importance of this fact in steering and diffraction of acoustic beams has been well recognized [1,2]. However, in solid state acoustics, where acoustic waves are traditionally generated by planar transducers, it has been long considered a "second-order" effect. The situation changes dramatically for the propagation from a point-like source. The most striking fact is that the acoustic wavefront (or group-velocity surface) can have a complicated shape with cusps and self-intersections [3]. Cuspidal edges yield sharp maxima in the acoustic intensity, the phenomenon termed "phonon focusing" [4,5]. Although the existence of cusps in the acoustic group velocity has long been known [1], the

first experimental observation was made not in acoustics but in experiments with ballistic thermal phonons [5]. It was only in the last decade that propagation from point sources at ultrasonic frequencies attracted substantial attention [6–8]. This attention was stimulated by the point-source/point-receiver approach in ultrasonic characterization of anisotropic materials [9,10] as well as by the development of ultrasonic techniques such as acoustic microscopy and laser ultrasonics making it easy to create point-like acoustic sources.

For surface acoustic waves (SAWs), phonon focusing effects and cuspidal wavefront structures were also predicted [11–13], and, more recently, observed experimentally with laser generated SAWs [14–17]. Imaging of anisotropic SAW wavefronts propagating from a point source attracted attention of several groups [17–19]. The most recent work [20] presented animated images of propagating SAW wavefronts, with the most intricate pattern observed on strongly anisotropic $TeO_2(001)$.

[a] e-mail: `alex.maznev@philips.com`
[b] On leave from the General Physics Institute, 117942 Moscow, Russia

In the present work, we expand the study reported in our earlier note [17] to give a systematic consideration of the main features encountered in anisotropic propagation of SAWs from a point source, using the results obtained for the (111) and (001) surfaces of GaAs to illustrate the main points. Our experimental method based on laser generation and detection of SAWs [21] provides adequate sensitivity for measurements in the far field, with the ratio of the source-to-receiver distance to the spatial length of a SAW pulse on the order of $\sim 10^3$. This allows us to resolve fine details of SAW wavefronts such as tiny cuspidal structures. Our calculation method also focuses on the far-field response, providing fast and efficient procedure involving only a one-dimensional numerical integration. We will also present analytical expressions for the shapes of SAW pulses corresponding to different sections of a wavefront with cuspidal structures, that agree well with the experimentally observed waveforms. In the asymptotic far-field expressions, the effect of phase velocity anisotropy, $i.e.$ phonon focusing, is explicitly separated from the angular dependence of the SAW excitation and detection efficiency, particularly pronounced for the (100) surface GaAs as well as a number of other cubic crystals where SAW degenerates into a bulk transverse wave. We will also present experimental results and calculations of the pseudo-SAW branch near the $\langle 110 \rangle$ direction in the (001) plane, where we reveal an additional anisotropic effect $i.e.$ the angular dependence of attenuation. The discussion will be concluded by a comparison of our quantitative results with "powder patterns", a qualitative method used in earlier surface phonon focusing studies [15,16].

It should be noted that the scope of the present work is limited to linear SAW propagation. Strong anisotropic effects specific to non-linear propagation of high-amplitude SAWs were recently reported in reference [22].

2 Group velocity

The SAW wavefront propagating from a point source corresponds within a scale factor to a polar plot of the SAW group velocity $v_g(\varphi)$, also called the wave surface. The value v_g and angle φ of the SAW group velocity vector $\mathbf{v}_g = \nabla_{\mathbf{k}} \omega$ are expressed in terms of the value v_f and angle θ of the phase velocity by

$$v_g = v_f \left[1 + (dv_f/d\theta)^2 \right]^{1/2}, \qquad (1)$$

$$\varphi = \theta + \arctan\left(\frac{1}{v_f} \frac{dv_f}{d\theta} \right). \qquad (2)$$

For a given wavevector $\mathbf{k}$, the group velocity vector is normal to the constant frequency surface $\omega(\mathbf{k}) =$ const. coinciding within a scale factor to the so-called "slowness surface" $i.e.$ the polar plot of the slowness $s = 1/v_f(\theta)$. If $1 + v_f^{-1}(d^2 v_f/d\theta^2) < 0$ for some interval of angles, then the corresponding section of the slowness surface is concave, with the result that different wavevectors may yield group velocities in exactly the same direction. This gives rise to a folded wave surface with cusps corresponding to
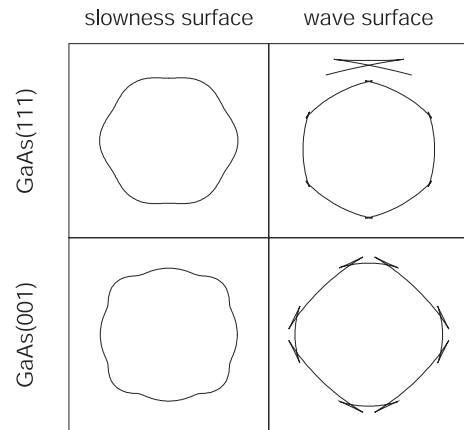
Fig. 1. Slowness and wave surfaces for SAWs in the (111) and (001) planes of GaAs. The vertical direction is $\langle 11\bar{2} \rangle$ in the former and $\langle 100 \rangle$ in the latter case. A tiny cuspidal structure in the wave surface for the (111) plane is shown with a magnification in the insert.

the inflexion points of the slowness surface. The existence of cusps is thus determined by the anisotropy of the phase velocity which, in turn, depends both on the elastic constants of the medium and the surface orientation [23]. Calculated slowness and wave surfaces for SAWs on the (111) and (001) planes of GaAs are shown in Figure 1. In the (111) plane, the slowness surface is only slightly concave near the $\langle 11\bar{2} \rangle$ direction resulting in a rather tiny cuspidal structure, while in the (001) plane more pronounced cusps can be seen.

Deviation of the group velocity from the wavevector also results in acoustic energy anisotropy described by the phonon-focusing factor [12,15,24]

$$A = \left| \frac{d\varphi}{d\theta} \right|^{-1} = \frac{1 + v_f^{-2}(dv_f/d\theta)^2}{\left| 1 + v_f^{-1}(d^2 v_f/d\theta^2) \right|}. \qquad (3)$$

At the cuspidal points, where $1 + v_f^{-1}(d^2 v_f/d\theta^2) = 0$, the focusing factor becomes infinite yielding caustics in the SAW intensity. Going beyond the ray approximation and taking into account the finite SAW wavelength λ shows [11,13,15] that in the caustic direction the SAW amplitude falls off with distance as $r^{-1/3}$ in contrast to the usual $r^{-1/2}$ dependence in other directions. This results in a sharp maximum of the amplitude in the far field $i.e.$ when $r/\lambda \gg 1$.

3 Surface response to a localized pulsed force: far-field calculation method

As it will be described in the following section, in our experiment SAWs are generated via laser ablation mechanism $i.e.$ due to a recoil pressure pulse acting on the sample surface. The problem of the displacement response of an elastic half space to a concentrated pulsed force, also known as the "Lamb problem", has recently attracted renewed attention in applications to anisotropic

solids [25,26]. Algorithms for calculating surface space-time Green's functions, yielding the surface displacement response to an instantaneous point force applied to the surface, have been developed for both free surfaces [26] and interfaces [27]. With the help of Green's functions, the surface displacement response to any model excitation source can be calculated *via* a convolution procedure. An alternative approach of using numerical finite-differences methods is becoming more attractive as the performance of computers improves. Both the Green's functions method [27] and finite-difference time-domain method [28] have been used successfully to model anisotropic SAW propagation at relatively small distances from the source, with $r/\lambda \sim$10–30. However, both approaches become increasingly computationally intensive as r/λ increases.

The exact response functions contain not only SAWs but also evanescent contributions of bulk waves falling off with distance much faster than SAWs [27,28]. In the far field these contributions can be disregarded, providing an opportunity to significantly simplify the calculations by taking into account only SAW and pseudo-SAW contributions to the response. A similar approach was adopted in reference [29] where the far-field response of the (001) surface of Si to a harmonic excitation force was calculated. Here, we present an algorithm for calculating SAW waveforms produced by an impulsive excitation force for an arbitrary crystal symmetry and orientation. We will show that for a Gaussian excitation pulse, some of the integrations required to obtain a space-time response can be performed analytically, leaving a simple one-dimensional integration for numerical computation. In addition to yielding a very simple computational method, our approach provides some insight into the interplay of different anisotropic effects influencing SAW propagation from a point-like source.

We consider a semi-infinite anisotropic elastic continuum occupying the half-space $x_3 > 0$. The displacement field $\mathbf{u}(\mathbf{r}, t)$ is described by the equations of motion [1]:

$$\rho\frac{\partial^2 u_i}{\partial t^2} = C_{ijkl}\frac{\partial^2 u_l}{\partial x_j \partial x_k}, \tag{4}$$

where ρ is the material density and C_{ijkl} the elastic constant tensor. The boundary conditions at the free surface $x_3=0$ are given by

$$\sigma_{3i} = C_{3imn}\frac{\partial u_m}{\partial x_n} = -\delta_{i3}F(\mathbf{x}_\parallel, t). \tag{5}$$

Here σ_{ij} is the stress tensor, and the right-hand side of the equation represents the external vertical force, with $\mathbf{x}_\parallel=(x_1,x_2)$ representing the "in-plane" coordinate. Below, we will assume the temporal and spatial distribution of the excitation force to be Gaussian,

$$F(\mathbf{x}_\parallel, t) = F_0 \exp(-t^2/\tau^2)\exp(-r^2/a^2), \tag{6}$$

where $r=|\mathbf{x}_\parallel|$.

Performing a Fourier transform over time t and "in-plane" coordinates

$$\widetilde{\mathbf{u}}(x_3, k, \omega) = \int dx dt \mathbf{u}(\mathbf{x}, t)\exp(i\omega t - i\mathbf{k}\mathbf{x}_\parallel) \tag{7}$$

reduces the problem to an algebraic one. Solutions of this algebraic problem are known [26]; in particular, the surface Green's function G_{33}, *i.e.* the vertical surface displacement response to an instantaneous vertical point force $F = \delta(\mathbf{x}_\parallel)\delta(t)$, is given by

$$\widetilde{G}_{33}(\mathbf{k}, \omega) = -\frac{1}{i\omega}\Psi_{33}(\mathbf{s}), \tag{8}$$

where $\mathbf{s} = \mathbf{k}/\omega$, and

$$\Psi_{33}(\mathbf{s}) = \sum_n \frac{adj(\mathbf{M})_{n,3}U_3^{(n)}}{\det|\mathbf{M}|}, \tag{9}$$

$$M_{n,m} = \sum_{ij}C_{3mij}s_i^{(n)}U_j^{(n)}. \tag{10}$$

Here $s_{1,2}^{(n)} = k_{1,2}/\omega$, while $s_3^{(n)}$ and $\mathbf{U}^{(n)}$, $n = 1,..,3$ are given by those three out of the six solutions of the Christoffel equation

$$(C_{ijkl}s_j s_k - \rho\delta_{il})U_l = 0, \tag{11}$$

which correspond to "outgoing" waves [23].

For a general source function $F(x, t)$ the Fourier-domain vertical surface displacement response is given by the product $\widetilde{F}(k, \omega)\widetilde{G}_{33}(k, \omega)$. Consequently, the space-time response is given by an inverse Fourier transform:

$$u_3(\mathbf{x}_\parallel, t) = \frac{1}{8\pi^3}\int d\mathbf{k}d\omega\widetilde{F}(\mathbf{k}, \omega)\widetilde{G}_{33}(\mathbf{k}, \omega)\exp(i\mathbf{k}\mathbf{x}_\parallel - i\omega t). \tag{12}$$

Equation (12) yields the exact formal solution to the time-domain problem. Now our goal is to simplify the integral to enable efficient computation of the far-field response.

First, we switch to the polar coordinates, $\mathbf{x}_\parallel \rightarrow (r, \varphi)$, $\mathbf{k} \rightarrow (k, \theta)$. Taking into account equation (8) and restricting the integration over ω to the interval $[0, +\infty]$ we get the result that

$$u_3 = \frac{1}{4\pi^3}Re\int_0^{+\infty}d\omega\int_0^{2\pi}d\theta$$
$$\times \int_0^{+\infty}dk\frac{k}{i\omega}\widetilde{F}(k, \theta, \omega)\Psi_{33}(s, \theta)$$
$$\times \exp[ikr\cos(\theta - \varphi) - i\omega t]. \tag{13}$$

We first consider the integration over k. Ψ_{33}, considered as a function of complex k, has a pole on the real axis due to the Rayleigh wave at $k_R = s_R(\theta)\omega$, where $s_R(\theta)$ is the Rayleigh wave slowness. Convergence of the integral is achieved by introducing infinitesimal "artificial damping" that shifts the pole off the real axis in accordance with

$$\frac{1}{k - k_R} \longrightarrow \frac{1}{k - k_R - i0}. \tag{14}$$

The far field response can be evaluated as the residue at the pole yielding the result that

$$u_3 = \frac{1}{2\pi^2} Re \int_0^{+\infty} d\omega$$

$$\times \int_{\varphi-\pi/2}^{\varphi+\pi/2} d\theta \; s_R(\theta) i\omega \widetilde{F}(k = s_R\omega, \theta, \omega)$$

$$\times R_{33}(\theta) \exp\left(i\omega[s_R(\theta)r\cos(\theta - \varphi) - t]\right), \quad (15)$$

where $R_{33}(\theta) = -iRes\Psi_{33}(s,\theta)|_{s=s_R}$ describes the anisotropy in the SAW generation efficiency in the **k** space.

For the Gaussian space-time source function of equation (6) the integration over ω can now be easily performed. Taking into account the fact that, in the vicinity of the SAW pole, Ψ_{33} is pure imaginary [26] and, consequently, $R_{33}(\theta)$ is real, we get the result

$$u_3 = F_0\tau a^2 \int_{\varphi-\pi/2}^{\varphi+\pi/2} d\theta \; s_R R_{33} \xi \tau_\theta^{-3} \exp\left(-\xi^2/\tau_\theta^2\right), \quad (16)$$

where

$$\xi = t - s_R r \cos(\theta - \varphi), \quad \tau_\theta = (\tau^2 + s_R^2 a^2)^{1/2}. \quad (17)$$

Equation (16), which is the main result of this section, contains only a simple one-dimensional integration and is easy to implement numerically. Note that the slowness curve $s_R(\theta)$ and $R_{33}(\theta)$ need to be computed only once for a given crystal surface, and can then be used to compute the response for any space-time point.

In the limit of large r, an alternative approach to calculating the integral in equation (15) is to use the stationary phase technique to perform the integration over θ. This procedure is well documented in the literature [11,13,15], so we only present the final result:

$$u_3 = \sum_j \frac{1}{(2\pi^3 r v_f^3)^{1/2}} \left[\frac{[1 + v_f^{-2}(\partial v_f/\partial\theta)^2]^{1/2}}{\left|1 + v_f^{-1}(\partial^2 v_f/\partial\theta^2)\right|}\right]^{1/2}$$

$$\times R_{33}(\theta_j) \, \Phi_\pm(t - r/v_g) \quad (18)$$

where $\Phi_\pm(\xi) = \int_0^{+\infty} d\omega \, \omega^{1/2} \exp\left[-\omega^2\tau_0^2/4\right]\sin\left(\omega\xi \pm \frac{\pi}{4}\right),$ (19)

where the sign in the argument of the sin function corresponds to the sign of $1 + v_f^{-1}(\partial^2 v_f/\partial\theta^2)$, i.e. to the sign of the slowness surface curvature. The SAW phase velocity $v_f = 1/s_R(\theta)$ and its derivatives are taken at stationary points $\theta = \theta_j$, determined by solving equation (2) with respect to θ. In the cuspidal region there are several solutions, so the response is given by the sum of contributions of different θ_j corresponding to a given observation angle φ. Finally, v_g is the group velocity determined by equation (1), and τ_0 is the duration of the SAW pulse,

$$\tau_0 = \left(\tau^2 + a^2/v_f^2\right)^{1/2}. \quad (20)$$
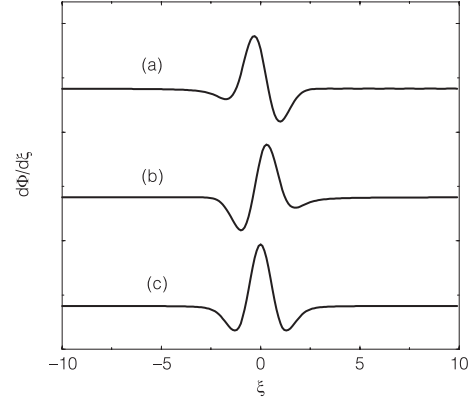
Fig. 2. Vertical surface velocity profiles in a SAW pulse according to equations (19) and (22) corresponding to (a) positive, (b) negative, and (c) zero curvature of the slowness surface.

At the cusp point, where $1 + v_f^{-1}(\partial^2 v_f/\partial\theta^2) = 0$, equation (18) becomes invalid. In this case, taking into account the next term in the series expansion of the phase in the stationary phase method [13,15] yields the contribution of a cusp point.

$$u_3 = \frac{F_0\tau a^2 3^{5/6}}{2^{2/3}\pi^2 v_f^{4/3} r^{1/3}} \left[\frac{[v_f^2 + (\partial v_f/\partial\theta)^2]^{1/2}}{|\partial v_f/\partial\theta + \partial^3 v_f/\partial\theta^3|}\right]^{1/3}$$

$$\times R_{33}(\theta_j) \, \Phi_0(t - r/v_g), \quad (21)$$

where

$$\Phi_0(\xi) = \int_0^{+\infty} d\omega \, \omega^{2/3} \exp\left[-\omega^2\tau_0^2/4\right] \, \cos\omega\xi. \quad (22)$$

While offering little advantage compared to equation (16) from the computational point of view, the asymptotic expressions (18) and (21) provide some insight into the behavior of the SAW response. First of all equations (19) and (22) yield analytical expressions for the shape of SAW pulses corresponding to the positive, negative, and zero curvature of the slowness curve. Note that in the experiment described in the following section we measured the slope $\partial u_3/\partial r$ rather than u_3 itself. Therefore the experimentally observed signal waveforms should be compared to the derivative $\partial\Phi/\partial\xi$. Figure 2 presents the plots of $\partial\Phi/\partial\xi$ for the three cases mentioned above. We notice that the waveforms corresponding to the positive and negative curvature of the slowness curve are "inverted in time" with respect to each other. The SAW pulse duration is determined either by the temporal or spatial width of the source function depending on whether τ or a/v_g is larger. The SAW amplitude anisotropy in equation (18) is determined both by the expression in square brackets, which describes the phonon focusing effect and almost coincides with the focusing factor as given by equation (3), and by the angular dependence of SAW generation and detection efficiency described by $R_{33}[\theta_j(\varphi)]$. Note that in the case of a line force [30], the anisotropy effect on the SAW amplitude is described solely by $R_{33}(\theta)$, in which case θ is the SAW wavevector direction perpendicular to the line along which the force is applied.

4 Experiment

The experimental set-up is represented in Figure 3. SAW pulses were generated by frequency-tripled (355 nm) Q-switched Nd:YAG laser irradiation, with the laser pulse duration and energy being 7 ns and 40 μJ, respectively. The laser beam was focused into a spot of 50 μm in diameter to produce surface heating and ablation accompanied by the generation of SAWs propagating away from the laser spot. The duration of the generated SAW pulses was mainly determined by the ratio of the laser spot size to the SAW velocity, *i.e.* ∼20 ns. The corresponding SAW frequency spectrum was thus limited to ∼50 MHz. At these frequencies, both room temperature acoustic attenuation and surface-roughness scattering on optical-quality polished GaAs samples were negligible for propagation distances of a few centimeters.

SAW waveforms were detected using the probe beam deflection technique [31]. The probe beam of a cw diode-pumped frequency-doubled Nd:YAG laser (532 nm) of 30 mW power was focused on the sample surface to a 10 μm- diameter spot at a distance from the excitation point of 3.21 or 2.51 cm for measurements on the (111) and (001) GaAs surfaces, respectively. The deflection angle of the reflected probe beam was detected by an arrangement of two fast photodiodes sensitive to the beam position. The signal, proportional to the surface slope and hence to the vertical surface velocity in a SAW pulse, was preamplified and recorded by a digital oscilloscope. The setup was able to detect a surface slope of 5×10^{-6} rad in the single-shot regime, which corresponded to about 0.1 nm surface displacement in a SAW pulse. The temporal resolution was ∼4 ns, being mainly limited by the finite size of the probe laser spot.

The excitation laser fluence was only slightly above the ablation threshold, therefore the shape of the SAW waveforms did not change over the first 100 laser shots used for averaging in order to improve the signal-to-noise ratio. To carry out measurements at different observation angles, the sample was rotated about an axis normal to the surface while the laser beams remained in place. Thus a fresh point on the sample was used for SAW excitation at each observation angle.

5 Results and discussion

5.1 SAWs on GaAs (111)

Figure 4a presents SAW waveforms on the (111) surface of GaAs recorded at different observation angles with respect to the $\langle 11\bar{2} \rangle$ direction. Two or three pulses corresponding to different branches of the cuspidal structure were observed at angles $|\varphi| \leq 4.5°$. The tiny cuspidal structure is well resolved due to the fact that the ratio of the SAW time-of-flight to the SAW pulse duration is as large as ∼10^3. At $\varphi = 0°$ the intersection of two branches of the wave front results in doubling of the amplitude of the second SAW arrival. This fact was used by us for the accurate
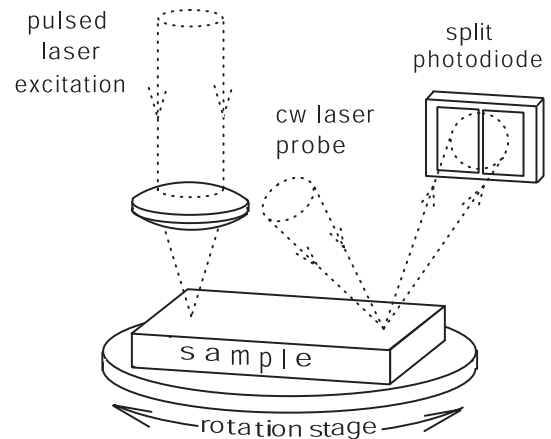

Fig. 3. Experimental set-up. SAW pulses were excited *via* surface ablation by focused nanosecond laser pulses and detected by the deflection of a cw probe beam measured by a fast split photodiode.

determination of the $\langle 11\bar{2} \rangle$ direction. When the observation direction deviates from $\langle 11\bar{2} \rangle$ by more than 0.2°, three SAW arrivals can be discriminated. With a further increase in the observation angle, the second arrival merges with the first one resulting in a pulse of enhanced amplitude with a maximum at about 2.5°. Subsequently, its amplitude falls off rapidly, and for $\varphi \geq 5°$ only a single SAW arrival can be observed.

Figure 4b shows the SAW waveforms calculated using equation (16) for $\tau = 4$ ns, corresponding to the FWHM laser pulse duration of 7 ns, $a = 25$ μm, and the same source-to-receiver distance as used in the experiment. The following values of GaAs elastic constants and density (see Ref. [32]) were used for all calculations in this work: $C_{11} = 118$ GPa, $C_{12} = 53.5$ GPa, $C_{44} = 59.4$ GPa, $\rho = 5.316$ g/cm^3. It should be noted that elastic constants of GaAs cited in different sources [1,32,33] vary by as much as 1%. This exceeds by an order of magnitude the piezoelastic stiffening effect [33], thus rendering unnecessary the incorporation of piezoelasticity into the calculations.

Note that for the ablation regime of SAW generation the spatial and temporal distribution of the recoil pressure acting on the surface is, in fact, unknown. We replaced it by the distribution of the laser intensity, which is obviously a very rough approximation. Nevertheless, the agreement between measured and calculated waveforms is very good. The calculations reproduce all features observed in the experiment such as different shapes of SAW pulses corresponding to different parts of the cuspidal structure and the enhancement of the first pulse amplitude near the cusp direction.

The measured angular dependence of the group velocity of SAW pulses is presented in Figure 5a while Figure 5b shows the angular dependence of the peak-to-peak amplitude of the SAW pulses. In general, measured and calculated group velocity data are in good agreement, with a slight systematic deviation being well within the uncertainty in the elastic constants of GaAs mentioned above.
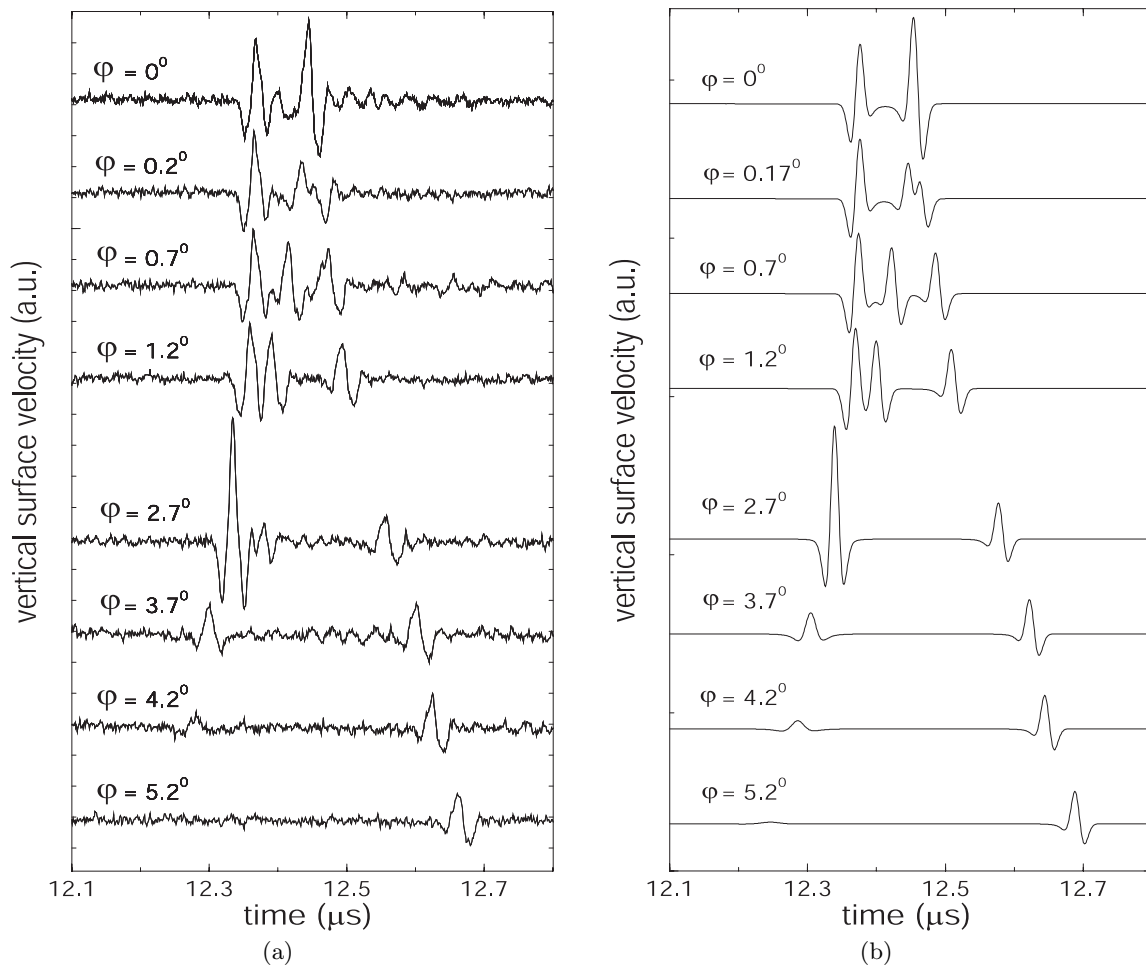
Fig. 4. (a) Measured and (b) simulated SAW waveforms at different angles to the $\langle 11\bar{2} \rangle$ direction on GaAs (111).
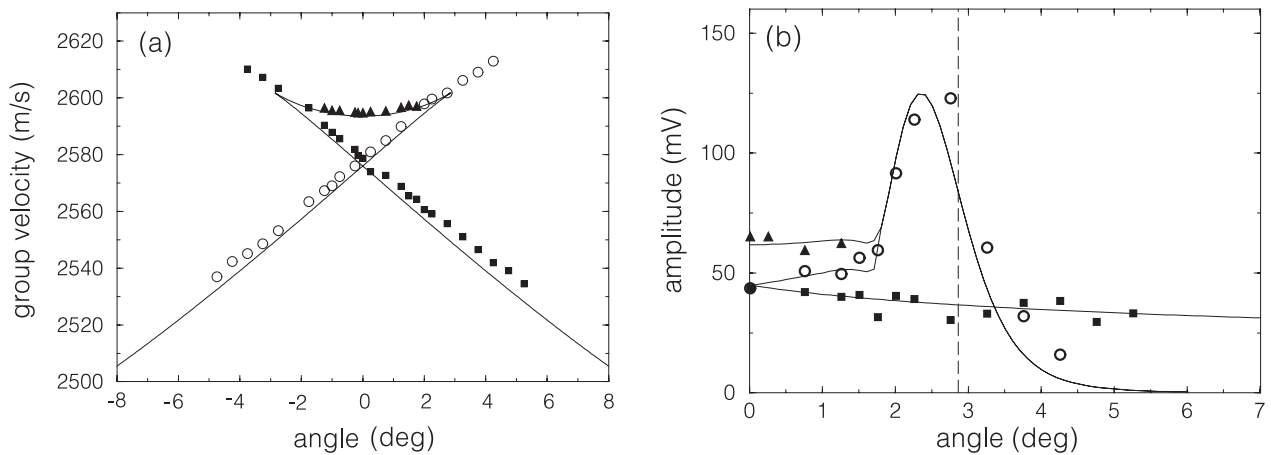
Fig. 5. (a) Measured angular dependence of the SAW group velocity on GaAs (111). The angle is measured from $\langle 11\bar{2} \rangle$. Triangles, open circles, and squares refer to different arrivals. The solid line is a theoretical curve calculated with equations (1) and (2). (b) Angular dependence of the peak-to-peak amplitude of the SAW pulses. The same symbols as in (a) are used for different arrivals. For $\varphi = 0°$ half of the measured amplitude of the second SAW arrival, resulting from the superposition of two pulses, is used. Solid lines represent theoretical results calculated from the simulated waveforms. The vertical dashed line marks the cusp location.
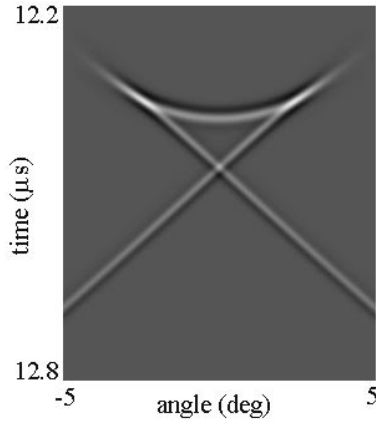
Fig. 6. Angle-time image of a SAW pulse on GaAs (111) calculated using equation (16). The angle is measured from $\langle 11\bar{2} \rangle$.

A remarkable finding, however, is that the first SAW arrival is detected well beyond the group velocity cusps lying at $|\varphi| = 2.9°$. This fact results from the restricted nature of the group velocity calculations corresponding to the geometrical acoustics approximation in which $\lambda/r \rightarrow 0$. Finite wavelengths lead to the phenomenon of "internal diffraction" [8] resulting in the penetration of the acoustic field beyond the cusps. This phenomenon was previously observed in group velocity measurements with bulk acoustic waves and termed "eidolon" [7]. As can be seen from Figure 4b, the eidolon is well reproduced by the far-field surface response calculations. A good illustration of the eidolon effect is provided by the simulated angle-time image of the cuspidal structure presented in Figure 6. The image is very similar to the group velocity surface, but instead of sharp cusps we have a steadily decaying response penetrating well beyond the caustics. The phonon focusing effect can clearly be seen in the enhancement of the amplitude near the cusps. The calculated angular dependence of the SAW amplitude shown in Figure 5b yields a quantitative picture and, again, demonstrates an agreement between the measurements and simulation. Note that for the (111) plane of GaAs, $R_{33}(\theta)$ is almost independent of the angle, therefore the SAW amplitude anisotropy is determined by the phonon focusing effect alone. Below we will see that this is not always the case.

5.2 SAWs on GaAs (001)

Results of measurements on the (001) GaAs surface are presented in Figures 7–8. Here, the measurements were made in a wider angular range and reveal a wide range of phenomena. First, near the $\langle 110 \rangle$ direction there is an additional leaky mode termed pseudo-SAW, or PSAW [23]. This mode slightly attenuates due to the coupling to a bulk transverse wave except for isolated directions of the wavevector for which it becomes a pure surface mode. The PSAW wavefront does not have cusps [34] but there is appreciable focusing in the $\langle 110 \rangle$ direction. Turning now to the SAW mode, we notice that the experimental data map
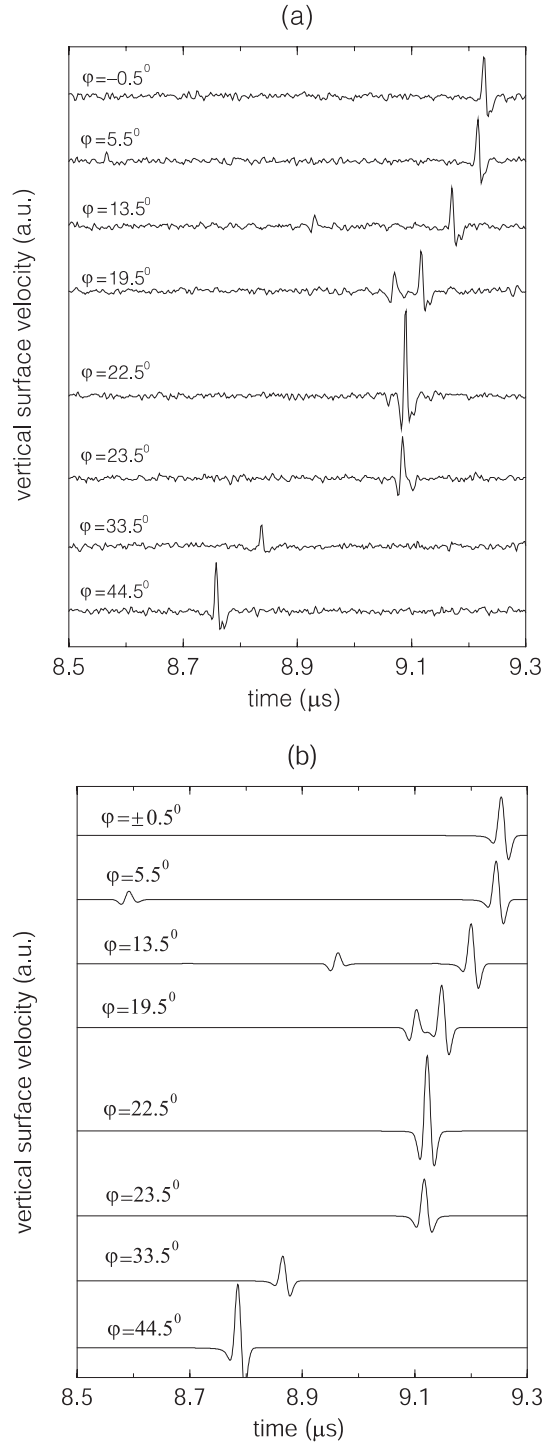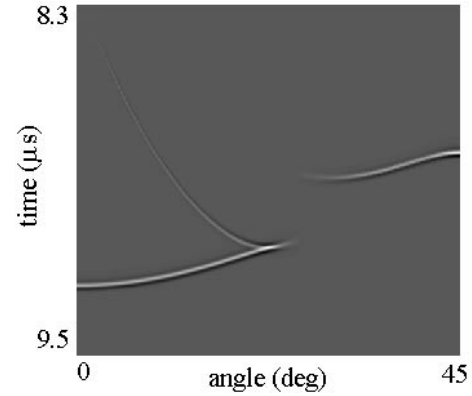

Fig. 7. (a) Measured and (b) simulated SAW waveforms on GaAs (001). The angle is measured from $\langle 100 \rangle$.

only a part of the wavefront, and only one SAW caustic of the two theoretically calculated ones is observed. The reason for that, as will be explained in more details below, is the angular dependence of SAW polarization which becomes predominantly shear horizontal as the wavevector direction approaches $\langle 110 \rangle$. It should be noted that a similar phenomenon has been previously observed [15] and simulated by calculations [29] for the (001) surface of Si.
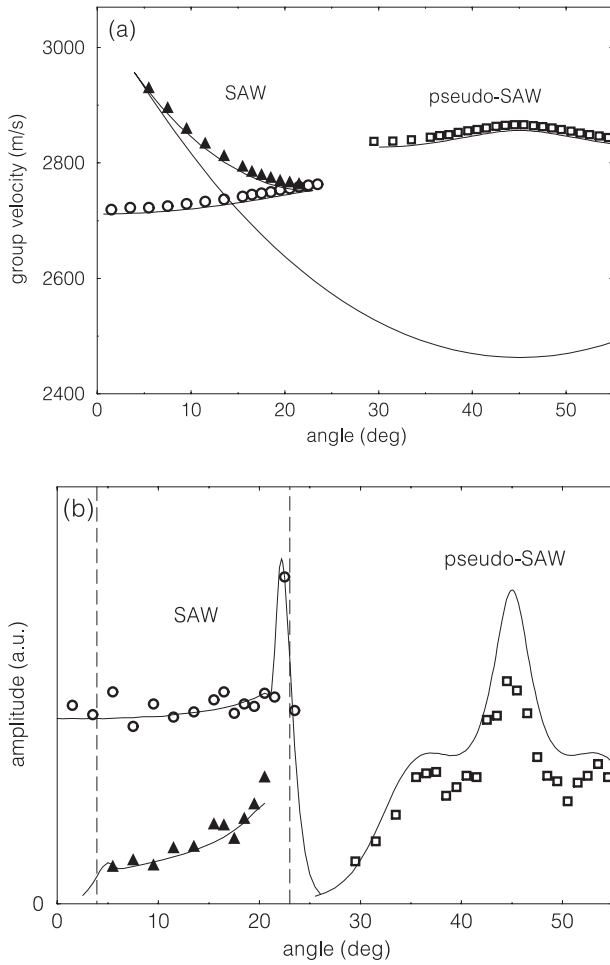
Fig. 8. (a) Measured and calculated angular dependence of the SAW and PSAW group velocity on GaAs (001). The angle is measured from $\langle 100 \rangle$. Triangles and open circles refer to different SAW arrivals. The solid line is a theoretical curve calculated with equations (1) and (2). (b) Angular dependence of the peak-to-peak amplitude of SAW and PSAW pulses. The same symbols as in (a) are used for different arrivals. Solid lines represent theoretical results calculated from the simulated waveforms. Cusp positions are marked by vertical dashed lines.

Fig. 9. Calculated angle-time image of SAW and PSAW waveforms on GaAs (001). The angle is measured from $\langle 100 \rangle$.
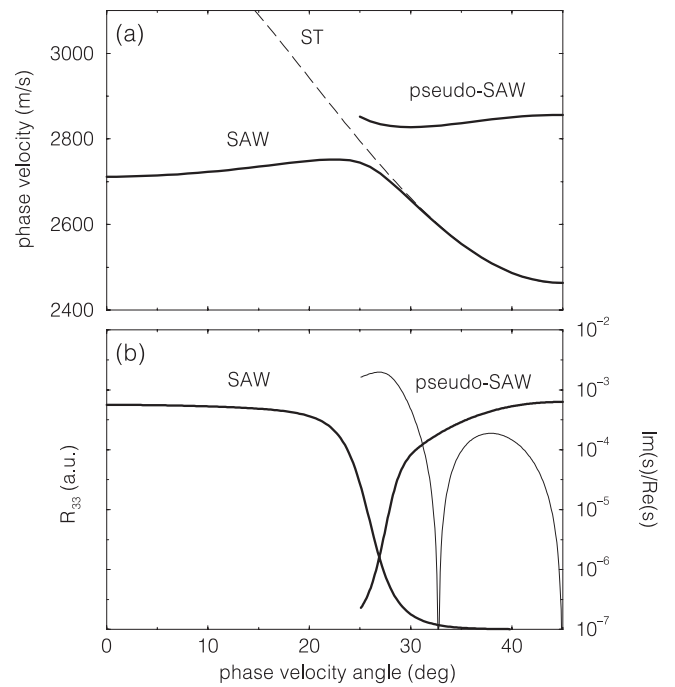
Fig. 10. Angular dependencies of (a) the phase velocity and (b) excitation/detection efficiency factor $R_{33}(\theta)$ for SAW and PSAW branches on GaAs (001). In (a), the dashed curve corresponds to the bulk slow transverse acoustic mode. In (b), the thin line shows the angular dependence of PSAW attenuation. The angle is measured from $\langle 100 \rangle$.

A comparison of the measured and calculated SAW waveforms (Fig. 7) as well as the measured and calculated angular dependencies of the SAW amplitude (Fig. 8b) shows a good agreement between theory and experiment. The calculated angle-time image is presented in Figure 9 and, in agreement with what is observed experimentally, a part of the calculated SAW wavefront in the image is missing. The reason for this behavior is that the SAW amplitude anisotropy is now determined not only by phonon focusing but also by the strong angular dependence of $R_{33}(\theta)$, resulting from the angular dependence of the SAW polarization pattern. It is known [23] that in cubic crystals, such as Si and GaAs, SAW on the (001) surface merges with the shear horizontal bulk wave as the phase velocity angle approaches 45° (*i.e.* the $\langle 110 \rangle$ direction), as illustrated in Figure 10a. Thereby the SAW po-

larization becomes predominantly shear horizontal while the SAW penetration depth into the substrate increases. Both factors diminish the vertical surface displacement in a SAW produced by a vertical surface force. As a result, $R_{33}(\theta)$ vanishes as θ approaches 45°, as shown in Figure 10b. Now it should be remembered that our observation angle is the group velocity angle φ rather than the phase velocity angle θ. The cuspidal points at $\varphi_1 = 23°$ and $\varphi_2 = 4°$ correspond to $\theta_1 = 21°$ and $\theta_2 = 29°$ in terms of the phase velocity angle. As can be seen in Figure 10b, R_{33} decreases sharply between θ_1 and θ_2 resulting in a decrease in the SAW amplitude. The whole section

of the SAW wavefront extending from the cuspidal point $\varphi_2 = 4°$ to the $\langle 110 \rangle$ direction and further (*i.e.* to a symmetric cuspidal point at $\varphi_2 = 86°$) is not observable because R_{33} quickly vanishes at $\theta > \theta_2$. One consequence of this fact is a "gap" at $\varphi \sim 26°$, where neither SAW nor pseudo-SAW signals could be detected.

It is interesting to compare Figure 9 to similar images for LiF(001) [20] as well as for the water-loaded Si(001) surface [19,27]. Both Si and LiF are cubic crystals similar to GaAs as far as elastic anisotropy is concerned, with the anisotropy factor $\eta = 2c_{44}/(c_{11} - c_{12})$ taking values of 1.57, 1.8, and 1.95 for Si, GaAs, and LiF, respectively. In the images of references [19,20,27], there is no gap between the SAW and PSAW branches, with the wavefront being seemingly continuous and the cusp in the SAW wavefront not well resolved. The reason is that those images correspond to relatively small source-to-receiver distances compared to the SAW wavelength, with $r/\lambda \sim 10$–30. In fact, for the case of a water-loaded surface, the attenuation of SAWs induced by the water loading broadens the SAW pulse thus limiting r/λ to about 30. That is, the far-field limit is never achieved, independently of how large the source-to-receiver distance is. Another consequence of this fact is a prominent near-field feature due to a bulk wave contribution in the images in references [19,27] that was not observed in our experiment.

5.3 Pseudo-SAWs on GaAs (001)

A PSAW is not a true surface wave in that it contains a small bulk wave component radiated from the surface, resulting in attenuation or "leakage" [23]. Mathematically, a PSAW corresponds to a pole in Ψ_{33} slightly shifted off the real axis of s, so that the slowness at the pole $s = s_R$ has a small imaginary part. Note that equation (16) used for the SAW response calculations was derived under the assumption of real s_R and real R_{33}. Consequently, it cannot be used to compute PSAW waveforms. On the other hand, stationary phase analysis retains its validity for a slightly complex slowness $s_R = s'_R + is''_R$. In this case, equation (18) should be replaced by

$$u_3 = \frac{1}{(2\pi^3 r v_f^3)^{1/2}} \left[\frac{[1 + v_f^{-2}(\partial v_f/\partial \theta)^2]^{1/2}}{\left| 1 + v_f^{-1}(\partial^2 v_f/\partial \theta^2) \right|} \right]^{1/2}$$

$$\times \mathrm{Re} \left[R_{33}(\theta_j) \int_0^{+\infty} d\omega\, (-i)\omega^{1/2} \exp\left(-\omega^2/\tau_0^2 - s''_R(\theta_j)\omega r \right.\right.$$

$$\left.\left. \times \cos(\theta_j - \varphi)\right) \exp\left(i\omega\xi \pm \frac{i\pi}{4}\right)\right], \quad (23)$$

where $v_f = 1/s'_R$ and all other notations are the same as in equation (18).

Since for the (001) surface of GaAs the PSAW slowness surface curvature is always positive, equation (23) can be used to calculate the PSAW contribution to the surface response for any observation angle. In this way, we obtained an angle-time image of the PSAW response shown along
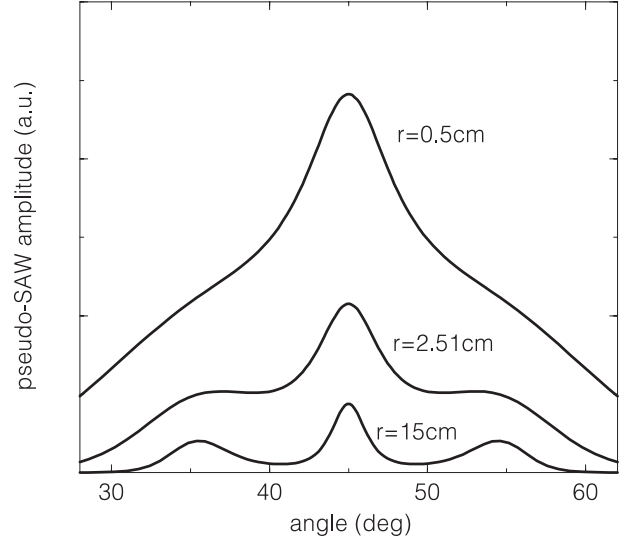
Fig. 11. Calculated angular dependence of the PSAW amplitude for different source-to-receiver distances. The angle is measured from $\langle 100 \rangle$.

with the SAW response in Figure 9, as well as the angular dependencies of the PSAW amplitude presented in Figure 8b. An interesting feature present in both calculated and experimental results is the presence of the "shoulders" in the angular dependence of the amplitude. It originates from the anisotropy in PSAW attenuation determined by the angular dependence of s''_R. There are isolated directions within the PSAW branch where s''_R vanishes. In these directions, the PSAW turns into a true surface wave. One such direction on GaAs(001) is well known [23] to be $\langle 110 \rangle$. However, there is another direction $\theta \simeq 33°$ corresponding to a group velocity angle $\varphi \simeq 36°$ at which s''_R also vanishes [35], as shown in Figure 10b. This anisotropy in s''_R results in a change in the angular dependence of the PSAW amplitude with observation distance, as illustrated in Figure 11. At a small source-to-receiver distance where the attenuation is not important, PSAW amplitude anisotropy is determined by phonon focusing and the angular dependence of R_{33}, both resulting in a maximum in the $\langle 110 \rangle$ direction, *i.e.* at $\varphi = 45°$. At larger distances the attenuation effect increases leading eventually to side maxima at $\varphi \simeq 36°$ and a symmetrical direction $\varphi \simeq 54°$.

5.4 Powder patterns

The angular dependence of the SAW amplitude can be visualized by "powder patterns" [14,16,36] formed by shake-off of small powder particles by high-amplitude SAWs. A focusing pattern for the (111) surface of GaAs obtained by this method has been presented and qualitatively explained in our previous work [15]. Now that we have quantitative measurements of the SAW amplitude *vs.* angle as well as a better understanding of the phenomena involved, it is instructive to compare the powder patterns for both (111) and (001) surfaces of GaAs with the new data.

The powder patterns are obtained by covering the sample surface with alumina particles of about 2 μm in diameter and exposing it to about 10 laser shots at a greater energy (about 1 mJ) than was used for the time-resolved measurements. Air flow directed at the surface helps obtain better patterns by removing the detached particles which otherwise tend to settle back onto the surface. Photographs of the resulting powder patterns on the (111) and (001) surfaces of GaAs are presented in Figure 12. Scattering of illumination light by particles makes a particle-covered surface look bright, while the areas where the particles were removed look dark. The degree of darkness in the images provides a qualitative indicator of the SAW amplitude.

The powder pattern on the (111) surface reveals a distinct pair of phonon focusing directions making an angle of about $\pm 2.5°$ with the $\langle 11\bar{2} \rangle$ direction. This angle is somewhat smaller than the 2.9° angle calculated for the geometrical caustics. This agrees with Figure 5b showing that the actual maximum of the SAW amplitude is closer to $\langle 11\bar{2} \rangle$ than the calculated cusp direction. The powder pattern also indicates that the SAW amplitude between the caustics is greater than outside, which also agrees with Figure 5b. Turning our attention to the powder pattern for the (001) surface, we see distinct focusing directions making an angle of $\simeq 22°$ with the $\langle 100 \rangle$ axis. This fact, again, is in agreement with the time-resolved measurements and the simulations, as is the absence of the maximum corresponding to another phonon focusing direction at $\varphi_2 = 4°$. The maximum at the $\langle 110 \rangle$ direction corresponding to the PSAW branch is also present in the powder pattern, and even the side shoulders resulting from the anisotropic attenuation appear to be reproduced. Also quite visible is a gap between the SAW and pseudo-SAW branches corresponding to a deep minimum in the surface response amplitude in Figure 8b.

6 Conclusions

The first objective of the present work was to study an amazing phenomenon in wave propagation in anisotropic media, *i.e.* cusps in the wavefronts propagating from point sources. This phenomenon has been previously studied with bulk acoustic waves. However, because of the complexity of three-dimensional slowness and wave surfaces, an explanation of the effect is usually given in terms of a two-dimensional picture [3]. Therefore, there is a general interest in a demonstration of this phenomenon for the two-dimensional surface wave propagation.

Furthermore, the present work provides a basis for the quantitative analysis of SAW waveforms in anisotropic materials. We have developed both a high-resolution experimental technique to measure SAW responses and a numerical algorithm to simulate them with good agreement between theory and experiment. Also, we have a clear understanding of the origin of different features in the SAW response. Although the study has been limited to the (111) and (001) planes of GaAs, it illustrates a variety of phenomena that can be encountered in the SAW propagation in anisotropic media. Besides general anisotropic
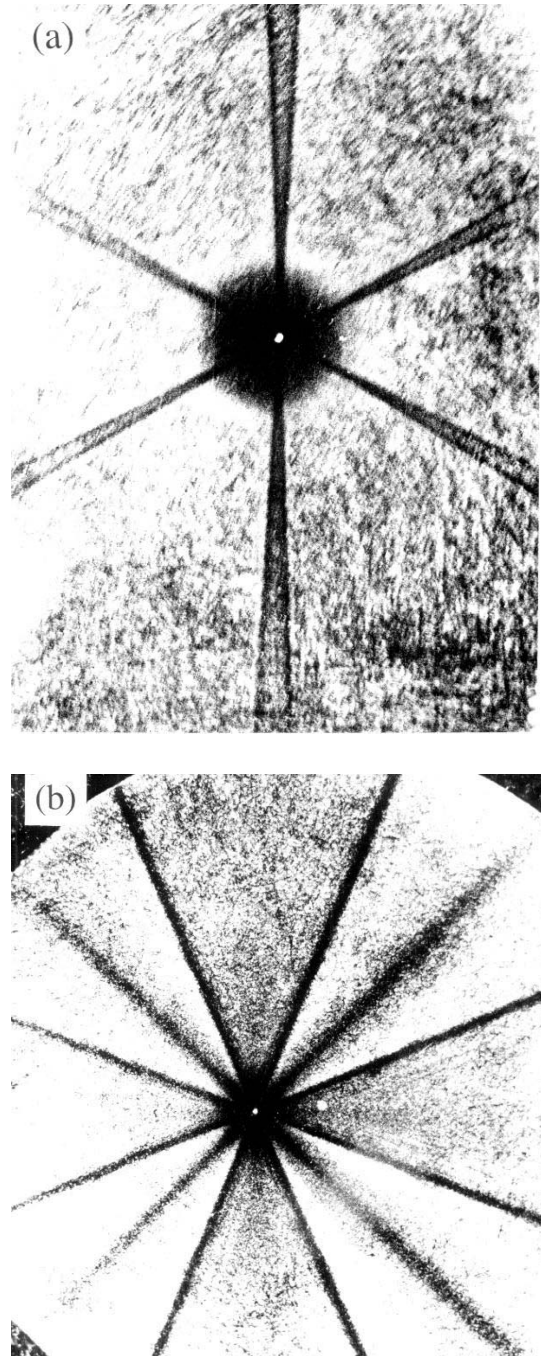
Fig. 12. Powder patterns on (a) (111) and (b) (001) surfaces of GaAs. The orientation of the images is the same as in Figure 1, *i.e.* the vertical direction is $\langle 11\bar{2} \rangle$ in (a) and $\langle 100 \rangle$ in (b).

wave propagation phenomena such as cusps in the group velocity, phonon focusing and internal diffraction, these include specific SAW effects such as a change in the polarization due to merging with a bulk mode and the presence of a pseudo-SAW branch with isolated pure-mode points.

Together with other work in the field [18–20, 25–28], this paper should be considered in the context of an effort to develop quantitative techniques to analyze the dynamic surface response of an elastically anisotropic solid.

At this point, adequate experimental and computational tools exist which allow to measure and simulate both near-field [19,26–28] and far-field responses, thus providing the necessary basis for using point-source/point-receiver surface acoustic techniques for materials characterization.

References

1. B.A. Auld, *Acoustic Fields and Waves in solids* (Wiley, N.Y., 1973)
2. T.L. Szabo, A.J. Slobodnik, Jr., IEEE Trans. Sonics Ultrason. **SU-20**, 240 (1973)
3. J.P. Wolfe, *Imaging Phonons* (Cambridge University Press, Cambridge, 1998)
4. B. Taylor, H.J. Maris, C. Elbaum, Phys. Rev. Lett. **23**, 416 (1969); Phys. Rev. B **3**, 1462 (1971)
5. G.A. Northrop, J.P. Wolfe, in *Nonequilibrium Phonon Dynamics*, edited by W.E. Bron (Plenum, NY, 1985)
6. A.G. Every, W. Sachse, K.Y. Kim, M.O. Thompson, Phys. Rev. Lett. **65**, 1446 (1990); A.G. Every, W. Sashse, Phys. Rev. B **44**, 6689 (1991); K.Y. Kim, W. Sashse, A.G. Every, Phys. Rev. Lett. **70**, 3443 (1993); K.Y. Kim, W. Sachse, J. Appl. Phys. **75**, 1435 (1994)
7. K.Y. Kim, K.C. Bretz, A.G. Every, W. Sachse, J. Appl. Phys. **79**, 1857 (1996)
8. M.R. Hauser, R.L. Weaver, J.P. Wolfe, Phys. Rev. Lett. **68**, 2604 (1992); R.L. Weaver, M.R. Hauser, J.P. Wolfe, Z. Phys. B **90**, 27 (1993); J.P. Wolfe, M.R. Hauser, Annalen der Physik 4, **99** (1995)
9. K.Y. Kim, W. Sachse, A.G. Every, J. Acoust. Soc. Am. **93**, 1393 (1993)
10. K.-U. Wurz, J. Wesner, K. Hillmann, W. Grill, Z. Phys. B **97**, 487 (1995)
11. V.T. Buchwald, Q.J. Mech. Appl. Math. **14**, 293 (1961); V.T. Buchwald, A. Davis, Q.J. Mech. Appl. Math. **16**, 283 (1963); H. Shirasaki, T. Makimoto, J. Appl. Phys. **49**, 658 (1978); **49**, 661 (1978); **50**, 2795 (1979)
12. S. Tamura, K. Honjo, Jap. J. Appl. Phys. **20**, Suppl. 20-3, 17 (1981)
13. R.E. Camley, A.A. Maradudin, Phys. Rev. B **27**, 1959 (1983)
14. Al.A. Kolomenskii, A.A. Maznev, JETP Lett. **53**, 423 (1991)
15. Al.A. Kolomenskii, A.A. Maznev, Phys. Rev. B **48**, 14502 (1993)
16. A.A. Maznev, A.G. Every, Solid State Commun. **97**, 679 (1996)
17. A.A. Maznev, Al.A. Kolomenskii, P. Hess, Phys. Rev. Lett. **75**, 3332 (1995)
18. T.-T. Wu, J.-F. Chai, Ultrasonics **32**, 21 (1994)
19. R.E. Vines, S. Tamura, J.P. Wolfe, Phys. Rev. Lett. **74**, 2729 (1995); R.E. Vines, M.R. Hauser, J.P. Wolfe, Z. Phys. B **98**, 255 (1995)
20. Y. Sugawara, O.B. Wright, O. Matsuda, M. Takigahira, Y. Tanaka, S. Tamura, V.E. Gusev, Phys. Rev. Lett. **88**, 185504 (2002)
21. A detailed discussion of laser excitation and detection of linear and nonlinear SAW pulses can be found in A.M. Lomonosov, P. Hess, A.P. Mayer, in *Modern Acoustical Techniques for the Measurement of Mechanical Properties*, edited by M. Levy, H.E. Bass, R. Stern (Academic Press, San Diego, 2001), pp. 65–134
22. A. Lomonosov, P. Hess, Phys. Rev. Lett. **83**, 3876 (1999)
23. G.W. Farnell, in *Physical Acoustics*, edited by W.P. Mason, R.N. Thurston, Vol. 6 (Academic Press, NY, 1970)
24. H.J. Maris, J. Acoust. Soc. Am. **50**, 812 (1971)
25. C.Y. Wang, J.D. Achenbach, Wave Motion **24**, 227 (1996); V.K. Tewary, C.M. Fortunko, J. Acoust. Soc. Am. 100, **86** (1996); A. Mourad, M. Deschamps, J. Acoust. Soc. Am. **97**, 3194 (1995); C. Bescond, B. Deschamps, J. Acoust. Soc. Am. **103**, 114 (1998)
26. A.G. Every, K.Y. Kim, A.A. Maznev, J. Acoust. Soc. Am. **102**, 1346 (1997)
27. A.G. Every, A.A. Maznev, G.A.D. Briggs, Phys. Rev. Lett. **79**, 2478 (1997)
28. Y. Tanaka, M. Takigahiro, S. Tamura, Phys. Rev. B **66**, 075409 (2002)
29. S. Tamura, M. Yagi, Phys. Rev. B **49**, 17378 (1994)
30. A.A. Maznev, A.G. Every, Int. J. Engng. Sci. **35**, 321 (1997)
31. H. Coufal, K. Meyer, R.K. Grygier, P. Hess, A. Neubrand, J. Acoust. Soc. Am. **95**, 1158 (1994)
32. *Landolt-Börnstein, New Series,* Group III, Vol. 29, edited by D.F. Nelson (Springer, Berlin, 1992)
33. *Akusticheskie Krystally (Acoustic Crystals), Handbook,* edited by M.P. Shaskol'skaya (Nauka, Moscow, 1982); *Landolt-Börnstein, New Series,* Group III, Vols. 1, 2, edited by K.-H. Hellwege, A.M. Hellwege (Springer, Berlin, 1966)
34. Depending on elastic anisotropy, pseudo-SAW wavefront on (001) cubic crystal surface may also contain cusps, see A.A. Maznev, A.G. Every, Acta Acustica **1**, 137 (1994)
35. G.I. Stegeman, J. Appl. Phys. **47**, 1712 (1976)
36. Al.A. Kolomenskii, A.A. Maznev, J. Appl. Phys. **77**, 6052 (1995)